Figure S1. Annual mean INP number concentrations as a function of freezing temperature observed at Tokyo Skytree, Japan, from August 2016 to July 2017 (Tobo et al., 2020) (black), and simulated for the corresponding location and period for dust only (red) and for all INP sources in the Base simulation (blue) and the observationally constrained simulation (purple). Gray shading indicates the range of observed INP number concentrations.
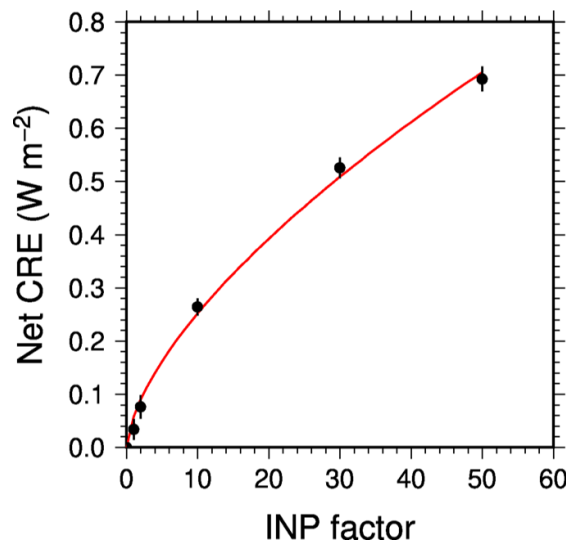
Figure S2. Relationship between INP scaling factors and net CREs via dust INPs estimated from the 1-, 2-, 10-, 30-, and 50-fold – 0-fold simulations. Dots and bars indicate the 10-year means and standard deviations of annual mean CREs. The red line represents the fitted power-law function ($y = ax^b$) used to infer the CREs corresponding to the 1-fold − 0-fold differences.
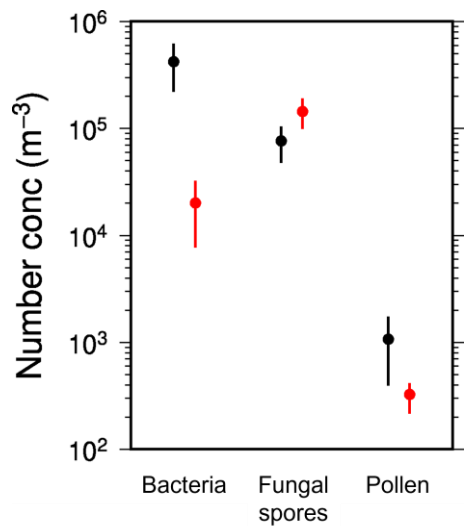
Figure S3. Bioaerosol number concentrations of bacteria, fungal spores, and pollen observed in northern Brazil (Patade et al., 2021) (black) and those simulated for the corresponding locations and periods (red). Dots and bars represent the averages and ranges during the observation periods, respectively.
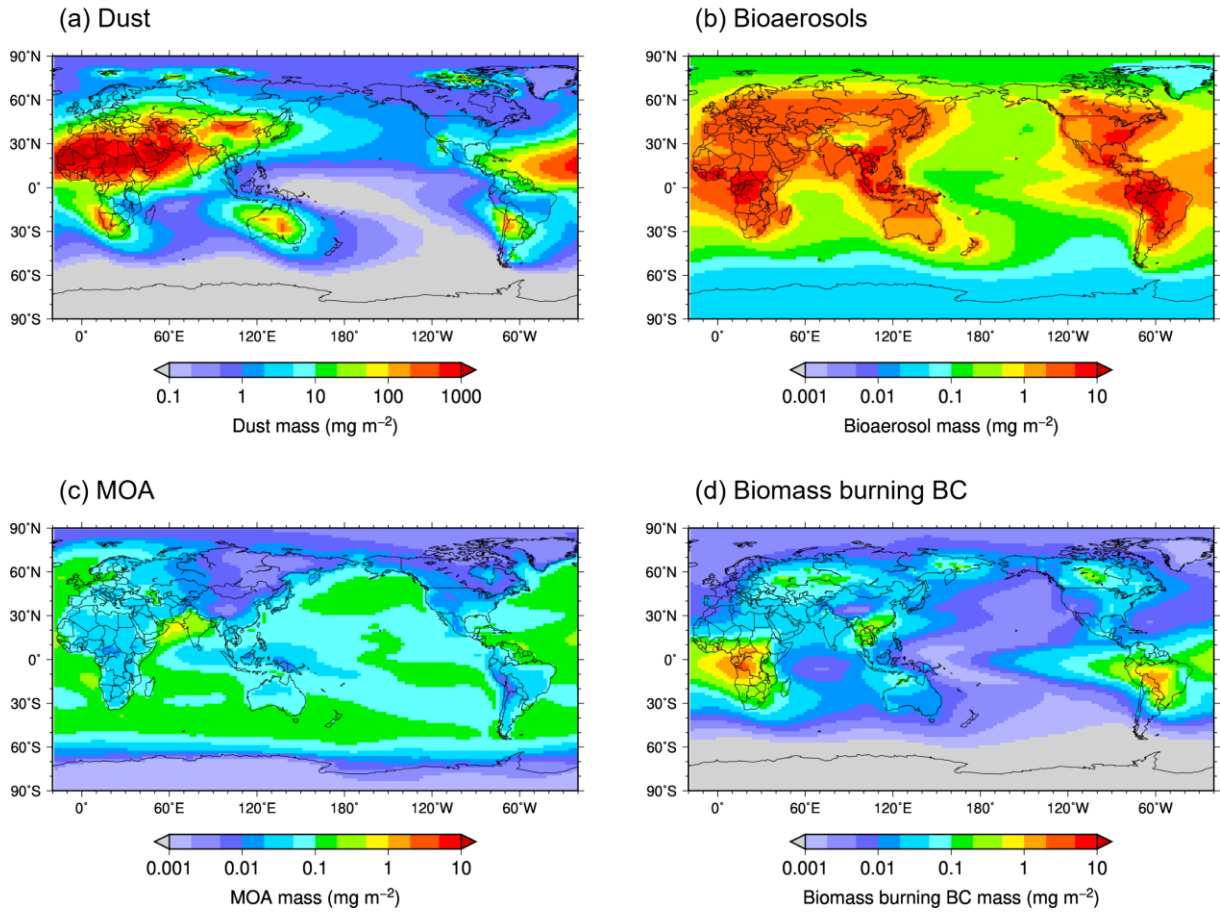
Figure S4. Annual mean vertically integrated mass concentrations of (a) dust, (b) bioaerosols, (c) MOA, and (d) biomass burning BC.
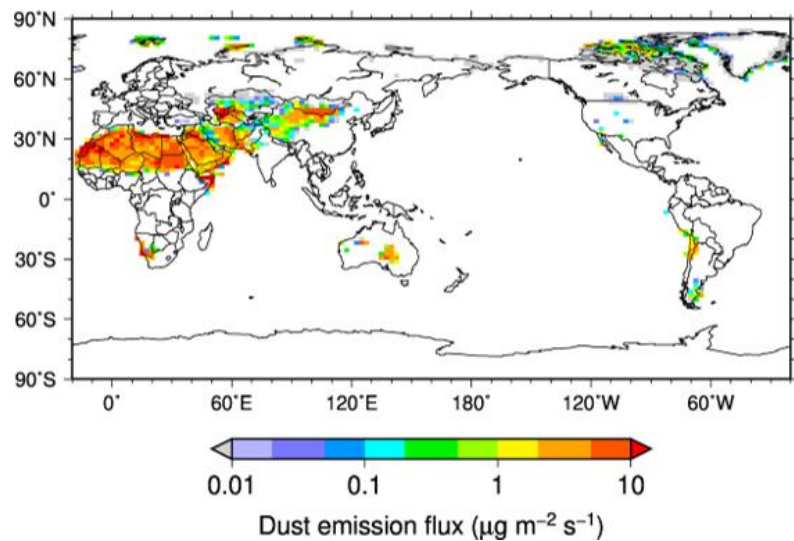
Figure S5. Annual mean dust emission fluxes simulated by the model.
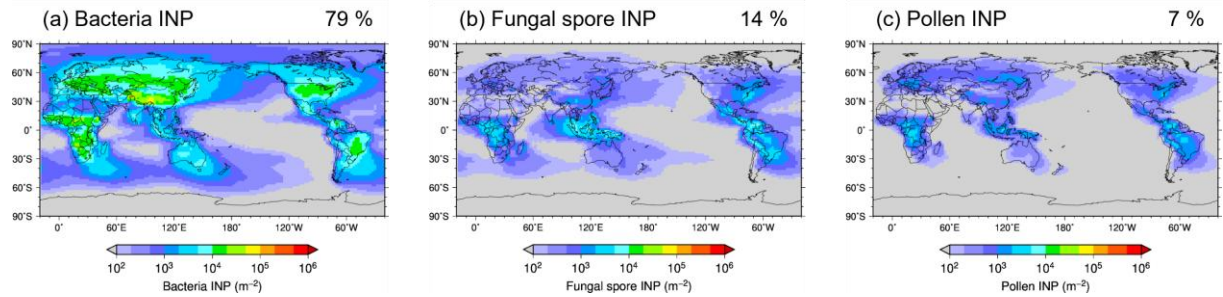
Figure S6. Annual mean vertically integrated INP number concentrations of (a) bacteria, (b) fungal spores, and (c) pollen. The proportion of each type in the global mean INP number concentration of bioaerosols (sum of these types) is indicated above each panel.
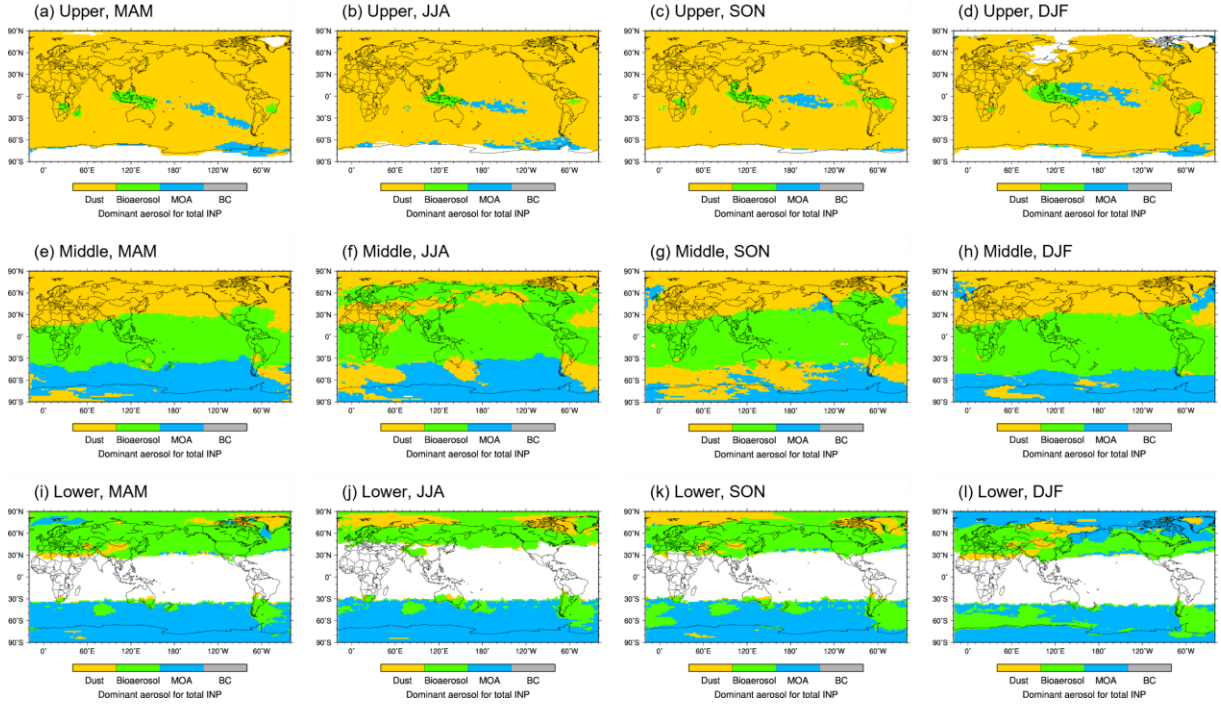
Figure S7. Dominant aerosol species contributing the largest fraction of seasonal mean vertically integrated total INP number concentrations in (a–d) the upper (100–400 hPa), (e–h) middle (400–700 hPa), and (i–l) lower troposphere (700–1000 hPa). Acronyms: MAM, March April May; JJA, June July August; SON, September October November; DJF, December January February.
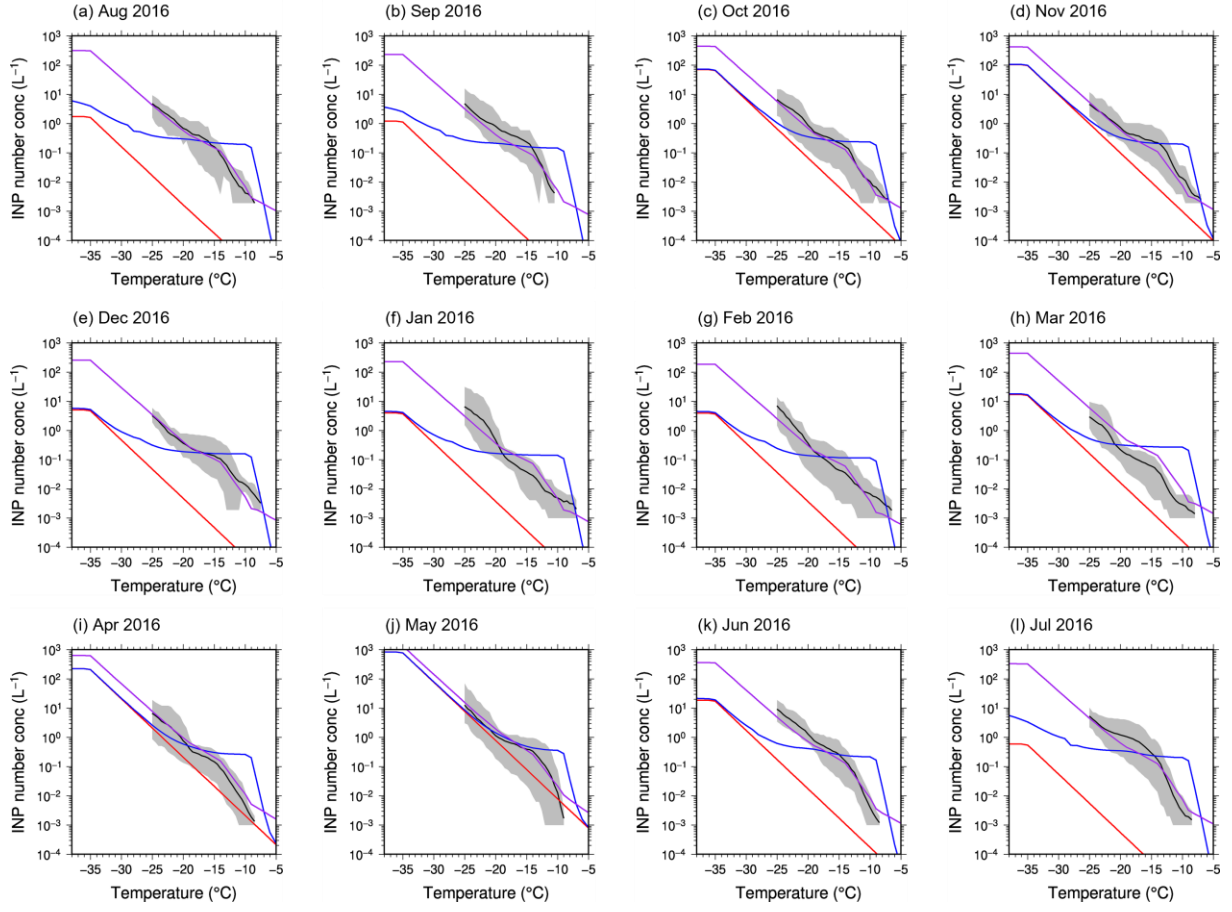
Figure S8. Monthly mean INP number concentrations as a function of freezing temperature observed at Tokyo Skytree, Japan, from August 2016 to July 2017 (Tobo et al., 2020) (black) and simulated for the corresponding location and period for dust only (red) and for all INP sources in the Base simulation (blue) and the observationally constrained simulation (purple). Gray shading indicates the range of observed INP number concentrations.
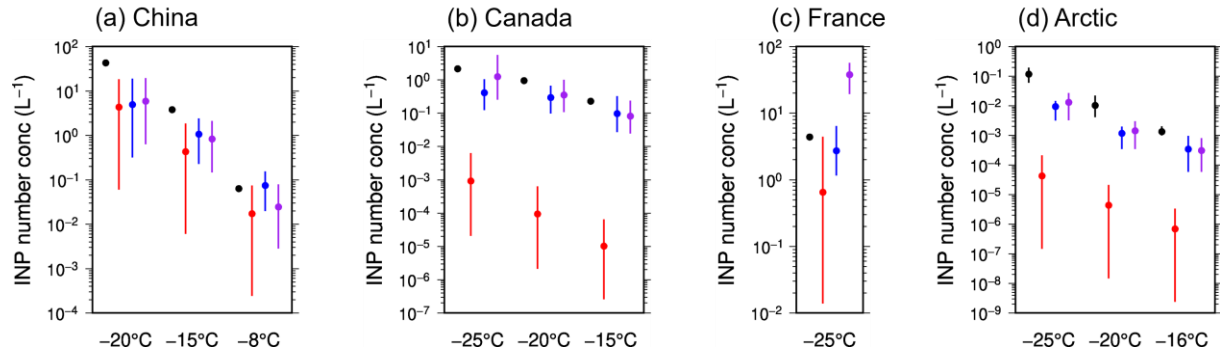
Figure S9. INP number concentrations observed at (a) Beijing, China (Hu et al., 2023); (b) Vancouver Island, Canada; (c) Saclay, France (Mason et al., 2016); and (d) Svalbard, Arctic (March 2017) (Tobo et al., 2019) at different freezing temperatures (black), and those simulated for the corresponding locations and periods for dust only (red) and for all INP sources in the Base simulation (blue) and the observationally constrained simulation (purple). Dots and bars represent the averages and ranges (where available), respectively, during the observation periods.

Table S1. Annual and global mean vertically integrated mass and INP number concentrations and their ratios for each aerosol species.

	Mass (g m^{-2})	INP number (m^{-2})	INP/mass (g^{-1})
Dust	6.1×10^{-2}	1.2×10^{5}	2.0×10^{6}
Bioaerosols	1.3×10^{-3}	3.1×10^{3}	2.4×10^{6}
MOA	7.4×10^{-5}	6.5×10^{2}	8.8×10^{6}
BC	2.1×10^{-4}	1.4×10^{2}	6.7×10^{5}

Table S2. Effects of dust, bioaerosols, and all aerosol species via INPs on annual and global mean cloud water path (g m^{-2}) for the Base and observationally constrained simulations estimated from the 10-fold − 1-fold simulations. The values represent the averages and standard deviations of the annual mean cloud water path for 10 years.

	Ice water path	Liquid water path	Total water path
Base simulation			
Dust INPs	0.49 ± 0.02	-0.65 ± 0.04	-0.16 ± 0.04
Bioaerosol INPs	0.0077 ± 0.0082	-0.10 ± 0.01	-0.093 ± 0.015
All INP sources	0.49 ± 0.03	-0.74 ± 0.03	-0.25 ± 0.03
Observationally constrained simulation			
All INP sources	1.2 ± 0.0	-1.9 ± 0.0	-0.70 ± 0.06

References

Hu, Y., Tian, P., Huang, M., Bi, K., Schneider, J., Umo, N. S., Ullmerich, N., Höhler, K., Jing, X., Xue, H., Ding, D., Liu, Y., Leisner, T., and Möhler, O.: Characteristics of ice-nucleating particles in Beijing during spring: A comparison study of measurements between the suburban and a nearby mountain area, Atmos. Environ., 293, 119451, https://doi.org/10.1016/j.atmosenv.2022.119451, 2023.

Mason, R. H., Si, M., Chou, C., Irish, V. E., Dickie, R., Elizondo, P., Wong, R., Brintnell, M., Elsasser, M., Lassar, W. M., Pierce, K. M., Leaitch, W. R., MacDonald, A. M., Platt, A., Toom-Sauntry, D., Sarda-Estève, R., Schiller, C. L., Suski, K. J., Hill, T. C. J., Abbatt, J. P. D., Huffman, J. A., DeMott, P. J., and Bertram, A. K.: Size-resolved measurements of ice-nucleating particles at six locations in North America and one in Europe, Atmos. Chem. Phys., 16, 1637–1651, https://doi.org/10.5194/acp-16-1637-2016, 2016.

Patade, S., Phillips, V. T. J., Amato, P., Bingemer, H. G., Burrows, S. M., DeMott, P. J., Goncalves, F. L. T., Knopf, D. A., Morris, C. E., Alwmark, C., Artaxo, P., Pöhlker, C., Schrod, J., and Weber, B.: Empirical Formulation for Multiple Groups of Primary Biological Ice Nucleating Particles from Field Observations over Amazonia, J. Atmos. Sci., 78, 2195–2220, https://doi.org/10.1175/JAS-D-20-0096.1, 2021.

Tobo, Y., Adachi, K., DeMott, P. J., Hill, T. C. J., Hamilton, D. S., Mahowald, N. M., Nagatsuka, N., Ohata, S., Uetake, J., Kondo, Y., and Koike, M.: Glacially sourced dust as a potentially significant source of ice nucleating particles, Nat. Geosci., 12, 253–258, https://doi.org/10.1038/s41561-019-0314-x, 2019.

Tobo, Y., Uetake, J., Matsui, H., Moteki, N., Uji, Y., Iwamoto, Y., Miura, K., and Misumi, R.: Seasonal Trends of Atmospheric Ice Nucleating Particles Over Tokyo, J. Geophys. Res.-Atmos., 125, e2020JD033658, https://doi.org/10.1029/2020JD033658, 2020.